

The quest for a stable disk

J. A. SELLWOOD¹ AND R. G. CARLBERG²

¹*Steward Observatory, University of Arizona
933 Cherry Avenue
Tucson, AZ 85722, USA*

²*Department of Astronomy and Astrophysics
University of Toronto
Toronto, ON M5S 3H4, Canada*

Submitted to ApJ

ABSTRACT

The majority of disk galaxies manifest spirals and/or bars that are believed to result from dynamical instabilities. However, some galaxies have featureless disks, which are therefore inferred to be dynamically stable. Yet despite many years of effort, theorists have been unable to construct realistic models of galaxy disks that possess no instabilities and therefore could remain featureless. This conclusion has been reached through simulations for the most part, some of which have been confirmed by linear stability analyses. Toomre claimed that the Mestel disk, embedded in an equal mass halo, to be a notable counter-example, but his prediction of stability could not be reproduced in simulations due to complicated non-linear effects that caused secular growth of Poisson noise-driven disturbances until strong features emerged. Here we revisit this issue and show that simply eliminating the most nearly circular orbits from Toomre’s disk model can inhibit troublesome secular growth. We also present both 2D and 3D simulations of particle disks that remain featureless for over 50 orbit periods. We report that spiral evolution naturally depletes circular orbits and that the radial velocity distribution in the featureless disks of S0 galaxies should have negative kurtosis.

Keywords: Spiral galaxies (1560) — Galaxy structure (622) — Galaxy dynamics (591) — Galaxy evolution (594)

1. INTRODUCTION

Because the stars of a disk galaxy generally move about the center in an ordered streaming flow with a small degree of random motion, we find that many disk galaxy models are beset by gravitationally-driven, collective instabilities. Bar-forming modes (Hohl 1971; Kalnajs 1978) are the most persistent, while others are edge modes (Toomre 1981; Papaloizou & Lin 1989), groove modes (Sellwood & Lin 1989; Sellwood & Kahn 1991), and buckling modes (Toomre 1966; Merritt & Sellwood 1994). We observe that most disk galaxies manifest spiral arms and more than half have either weak or strong bars (Erwin 2018), which are believed to result from instabilities (see Sellwood & Masters 2022, for a review). However, there are some that have neither, which challenge dynamicists to construct somewhat realistic models of disk galaxies

that are completely stable. Not only is this a challenge in its own right, but such models would be valuable to study responses to perturbations without the complication of intrinsic instabilities.

Yet, to our knowledge, only two types of stable, rotationally supported stellar disk models are known. The first stems from the classic study of uniformly rotating 2D disks by Kalnajs (1972), who was able to derive the full spectrum of normal modes of a class of models that rotated at a uniform rate Ω that was slower than the circular rate. All his single Ω models possessed some instabilities, but he was also able to construct composite models by superposing variously weighted single Ω models and found two cases that possessed no in-plane instabilities whatsoever. Unfortunately, not only is uniform rotation unrealistic, but the same models are unstable to buckling modes (Polyachenko 1977) when motion out of the plane is permitted.

The other case, presented by [Toomre \(1981\)](#), is the flattened half-mass Mestel disk which we fully describe in §2 below. Toomre was unable to find any instabilities in his linearized stability analysis, and therefore claimed that the disk should be stable. Note that the Mestel disk is also a 2D model that would suffer from buckling instabilities ([Merritt & Sellwood 1994](#)) if motion outside the disk plane were allowed, but buckling modes are suppressed in disks of finite thickness if the vertical velocity dispersion of the stars is $\gtrsim 1/3$ that of the radial dispersion ([Toomre 1966](#); [Araki 1987](#)).

[Sellwood \(2012, hereafter S12\)](#) tested Toomre’s prediction, and confirmed that his larger- N simulations of the initial model did not possess any *linear* instabilities. However, he found unexpectedly that simulations with even very large numbers of particles, up to 500 million, always manifested secular growth in two stages. At first, the leading components of the inevitable shot noise were amplified as they sheared to trailing. The amplified disturbance extracts energy from the gravitational well of the disk through outward angular momentum transport, which must later be absorbed at the Lindblad resonances ([Lynden-Bell & Kalnajs 1972](#); [Mark 1974](#)). The energy absorbed by the resonant particles is second order in the disturbance amplitude, changing, or “scratching,” the DF very slightly. The scratch is localized in angular momentum and increases the random energy of the resonant stars thereby creating a deficit of low- E_{rand} stars. Subsequent amplified noise is affected by previous scratches, causing responsiveness of the disk to grow gradually, and the general level of activity also to rise. Eventually, the scratches become deep enough to seed a true groove-type instability, at which point amplitude growth becomes exponential, leading to the appearance of a finite amplitude bar. [Fouvry & Pichon \(2015\)](#) were able to reproduce Sellwood’s findings using quasi-linear theory, even to predict, from Sellwood’s input noise spectrum, the frequency of the instability that eventually emerged ([De Rijcke, Fouvry & Pichon 2019](#)). There seems no reason that this sequence of events can be avoided no matter how many particles are employed, and therefore Toomre’s prediction of linear stability is undermined by non-linear resonant scattering.

[Sellwood & Carlberg \(2023\)](#) reviewed the extensive literature on bar instabilities, which we do not repeat here. The conclusions from their survey were that heavy halos do suppress bar instabilities in cool disks, but only to unleash multi-arm spiral instabilities in their place. Bar instabilities can also be quelled by raising Q , however no analytical requirement for non-axisymmetric stability is known. A survey of then available numerical results led [Athanasoula & Sellwood \(1986\)](#) to propose

that “ $Q \simeq 2 - 2.5$ at all radii as a sufficient criterion for non-axisymmetric stability”. However, as noted above, high radial velocity dispersion in disks mandates substantial vertical thickness to inhibit buckling instabilities, requiring an unrealistic degree of puffiness if full-mass disks are to be stable.

Here we continue the search for a more nearly stable disk model, by showing that the troublesome secular growth in the Mestel disk reported by S12 can be suppressed by a minor modification to the DF. Since the secular growth is caused by groove-type behavior, we must first highlight one property of groove modes that has not previously been emphasized, but which will be important to the solution we propose.

2. MESTEL DISK MODEL

The razor-thin Mestel disc used in the studies by [Zang \(1976\)](#) and [Toomre \(1981\)](#) is characterized by a constant circular speed V_0 at all radii, and has the mid-plane potential $\Phi(R) = V_0^2 \ln(R/R_0)$ where R_0 is a reference radius that defines the zero of the potential. The axisymmetric surface density, $\Sigma_0(R) = V_0^2/(2\pi GR)$, would self-consistently yield the appropriate central attraction for centrifugal balance for $0 \leq R \leq \infty$. [Toomre \(1977\)](#) and [Binney & Tremaine \(2008\)](#) give the DF for this disk that has a Gaussian distribution of radial velocities with spread σ_R at all radii:

$$f(E, L_z) = \begin{cases} F (L_z/R_0 V_0)^q e^{-E/\sigma_R^2} & L_z > 0 \\ 0 & \text{otherwise,} \end{cases} \quad (1)$$

where $q = V_0^2/\sigma_R^2 - 1$, and the normalization constant is

$$F = \frac{1}{GR_0} \frac{(q/2 + 0.5)^{q/2+1}}{\pi^{3/2}(q/2 - 0.5)!}. \quad (2)$$

[Zang \(1976\)](#) applied a central cutout to the disk, described below, in order to avoid difficulties with particles having near infinite frequencies as $L_z \rightarrow 0$, which he replaced by bulge-like rigid matter to preserve the central attraction $a_R = -V_0^2/R$ at all radii. His linear stability analysis of this centrally cut-out, but otherwise full-mass, disk revealed a persistent lop-sided ($m = 1$) instability no matter how gentle the central cutout. Therefore [Toomre \(1981\)](#) studied the stability of the same cutout model but with the active mass halved to suppress the lop-sided mode, with the removed mass replaced by rigid halo-like matter to preserve the disk equilibrium.

While maintaining the centripetal acceleration $a_R = -V_0^2/R$ everywhere, [Toomre \(1981\)](#) multiplied the DF (eq. 1) by the double taper function

$$T(L_z) = \left[1 + \left(\frac{R_0 V_0}{L_z} \right)^\nu \right]^{-1} \left[1 + \left(\frac{L_z}{R_1 V_0} \right)^\mu \right]^{-1}, \quad (3)$$

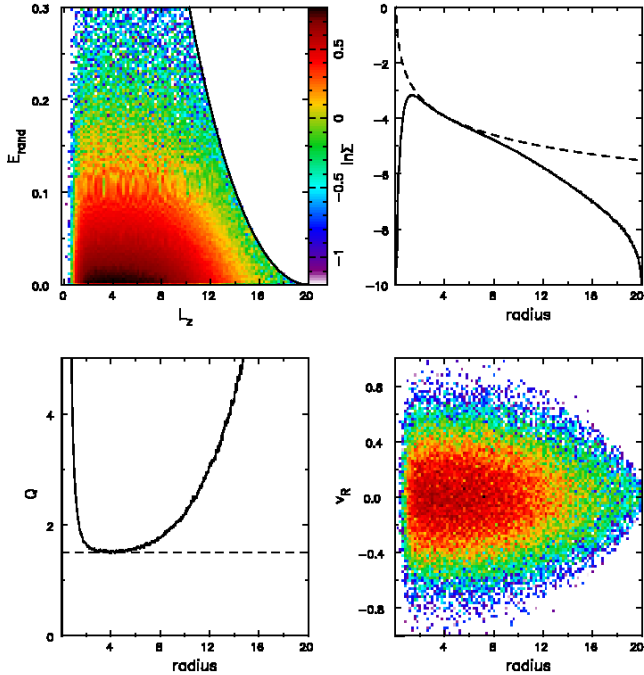


Figure 1. Properties of our standard DF for in the doubly-tapered, half-mass Mestel disk. Top left: The particle distribution in (L_z, E_{rand}) ; the solid line is the upper bound on energy imposed by restricting particle orbits to not stray beyond $R = 20$. Top right: The solid curve gives the active surface density of the disk, the dashed curve is what it would be without the tapers. Bottom left: The solid curve shows the radial variation of Q while the dashed curve shows the value Q would have in a disk lacking tapers. Bottom right: the distribution of radial velocities, for which $\sigma_R \simeq 0.284$ in the self-similar disk, but is lower in the very inner and outer parts due to the tapers.

to create the central cutout having mean radius R_0 , as well as an outer taper having mean radius R_1 to limit the radial extent of the otherwise semi-infinite disk. He chose $q = 11.44$ or $\sigma_R = 0.284V_0$ to ensure $Q \rightarrow 1.5$ outside the inner cutout of the half-mass Mestel disk. Setting the taper indices $\nu = 4$ and $\mu = 5$ yielded an idealized, smooth disc model that [Toomre \(1981\)](#) claimed possessed no small amplitude unstable modes. Here we choose $R_1 = 11.5R_0$, as did [S12](#), and further limit the radial extent of the disc by an energy cut-off to eliminate particles having sufficient energy to pass $R = 20R_0$. We shall refer to this DF, which was employed in [S12](#), as our “standard DF” and we adopt units such that $G = V_0 = R_0 = 1$.

Figure 1 presents some properties of our standard DF with the tapers and energy restriction applied to the function (1). The top left panel presents the density of particles in (L_z, E_{rand}) space, where

$$E_{\text{rand}} = E - E_c(L_z), \quad (4)$$

Table 1. Default numerical parameters for 2D

Grid points in (r, ϕ)	220×256
Grid scaling	$R_0 = 10$ grid units
Active sectoral harmonic	$m = 2$
Plummer softening length	$\epsilon = R_0/10$
Number of particles	5×10^6
Largest time-step	$0.08R_0/V_0$
Radial time step zones	5
Guard radii	4

is the excess of energy over that of a circular orbit of L_z and the right-hand boundary, delineated by the solid curve, marks the restriction that no particle has sufficient energy to pass $R = 20R_0$. Note that the typical random energy of a particle having $v_R = \sigma_R$ is $E_{\sigma_R} = \sigma_R^2/2 \simeq 0.04$. The surface density profile of the active disk is marked by the solid line in the top right panel, which closely matches the surface density of the untapered, half-mass disk (dashed curve) over the radial range $2 \lesssim R \lesssim 8$. The untapered disk would be self-similar with $Q = 1.5$ and $\sigma_R \simeq 0.284$ at all radii, but the radial velocities (bottom right panel) of the active particles are limited by both the inner and outer tapers. The solid curve in the bottom left panel shows the radial variation of Q measured from the surface density and velocity distribution of the active particles.

3. SIMULATION CODE

We select particles from the adopted DF using the procedure described in [Sellwood \(2024\)](#), place them in a plane at random azimuths and compute the mutual attractions of the particles using a 2D polar mesh. This code, which has been widely used and tested, is described in detail in [Sellwood \(2014\)](#); briefly the particles move subject to forces from other particles that are interpolated from the grid. We adopt the parameters listed in Table 1.

In the simulations we report here, the central attraction is always $a_R = -V_0^2/R$, which therefore includes the attraction of all rigid material as well as that of the mobile particles and, unless otherwise stated, only the $m = 2$ sectoral harmonic contributes to the non-axisymmetric terms. We employ block time steps that are decreased by factors of 2 in each radial zone and are further subdivided in a succession of guard zones near the bulge-dominated center where self-gravity of the disk is not updated at every sub-step.

As usual, we measure non-axisymmetric distortions of the distribution of the N particles using an expansion

in logarithmic spirals:

$$A(m, \gamma, t) = \frac{1}{N} \sum_{j=1}^N \exp[im(\phi_j + \tan \gamma \ln R_j)], \quad (5)$$

where (R_j, ϕ_j) are the polar coordinates of the j th particle at time t , m is the sectoral harmonic, and γ is the (radially constant) angle of the spiral component to the radius vector, which is the complement to the spiral pitch angle.

4. GROOVE MODES

Following Sellwood & Binney (2002), we multiply our standard DF (Fig. 1) by a Lorentzian function of L_z to create an axisymmetric groove

$$\mathcal{G}(E, L_z) = H(E_{\text{rand}}) \left[1 + \frac{\beta w_{L_z}^2}{(L_z - L_*)^2 + w_{L_z}^2} \right], \quad (6)$$

and generally choose the parameters: mean $L_* = 6.5R_0V_0$, depth $\beta = -0.4$, and width $w_{L_z} = 0.1R_0V_0$.

In the study by Sellwood & Binney (2002), H was set to unity and the groove extended over all bound values of E_{rand} . But more recent experience (*e.g.* Sellwood & Carlberg 2019) suggests that grooves among the low E_{rand} particles are the principal source of instability. Therefore we here study how groove instabilities are affected when we restrict the extent of the groove to low, or high, values of E_{rand} by setting $H = 0$ or 1, depending upon whether

$$E_{\text{rand}} \lesseqgtr E_{\text{rand,crit}}, \quad (7)$$

for various values of $E_{\text{rand,crit}}$.

Fig. 2 presents results from several simulations, two of which have been published before. The magenta line is from a simulation with no groove and uses identically the same initial DF, except for the random draw, as the $N = 5\text{M}$ particle run in S12. The raw measure from eq. (5) is plotted as the dotted line in each case and the heavily smoothed data are indicated by the solid lines. Fig. 2 of S12 used a different procedure to smooth the $m = 2$ amplitude, but the behavior was qualitatively the same as shown here. The measured amplitude is initially that expected from randomly placed particles, which is marked by the horizontal dashed line, but rises rapidly by about a factor of ten as the particle distribution becomes polarized (Toomre & Kalnajs 1991) due to the mutual attractions of the disk particles. Subsequently, the amplitude of the dotted magenta line fluctuates about the mean (solid line), as randomly excited transient spirals in different parts of the disk overtake one another causing alternating constructive

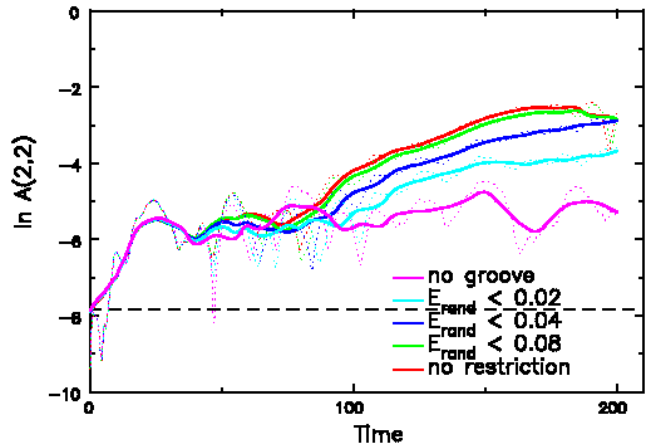


Figure 2. The dotted lines report the time evolution of the $m = 2$, $\tan \gamma = 2$ logarithmic spiral in a series of simulations having grooves present over the indicated range of E_{rand} in each case while the heavily smoothed values are marked by the solid curves. As the height of the groove in E_{rand} is increased from zero (magenta curve), the vigor of the instability increases until there is no upper E_{rand} bound on the groove (red curve). Notice that the instability is only mildly less vigorous when the groove is restricted to $E_{\text{rand}} < 2E_{\sigma R}$ (green curve) than when the groove is present for all E_{rand} (red curve).

and destructive interference in the measured amplitude. The duration of the simulations shown in Fig. 2 is too short to reveal the secular rise reported by S12, but it becomes apparent later – see §5.

The red line in Fig. 2 is from the model having a strong groove instability, that was employed by Sellwood & Binney (2002). The groove had the factor $H = 1$ in eq. (6) and therefore extended over all random energies. Although a narrow feature in L_z , random motion blurs the groove in radius, and since it cuts away just 1.1% of the disk mass, its effect on the Σ - and Q -profiles is barely detectable. The only differences are that here we employ half the groove width and 5M particles, whereas Sellwood & Binney (2002) used 6M. The groove instability causes the red line to emerge from the noise around $t \simeq 70$ and to rise roughly exponentially to saturation near $t \simeq 180$, a little earlier than in Sellwood & Binney (2002) because of the minor differences in the model.

4.1. Grooves among low E_{rand} particles only

Here we experiment by setting $H = 1$ when $E_{\text{rand}} < E_{\text{rand,crit}}$ and $H = 0$ otherwise, which creates a groove among the particles of low E_{rand} only.

The results from a series of runs in which the groove is restricted in this way to several values of $E_{\text{rand,crit}}$ are also presented in Fig. 2. The green curve mani-

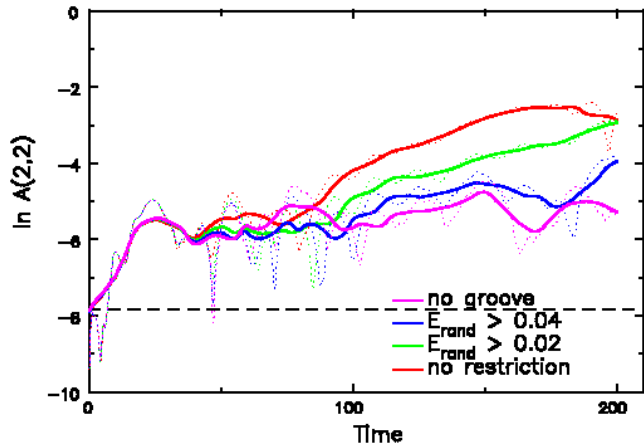


Figure 3. As for Fig. 2, but when the groove is present for higher random energies and not for lower. The red and magenta curves are the same in both figures.

festes almost the full instability when $E_{\text{rand,crit}} = 0.08$, implying that yet higher random energy particles take little part in the instability. The vigor of the instability decreases as the groove is restricted to lower E_{rand} . However, the cyan curve reveals that a mild instability still persists when the groove is restricted to as little as $E_{\text{rand,crit}} = 0.02$.

4.2. Grooves among high E_{rand} particles only

Fig. 3 shows the effect on the instability caused by a groove in only the most eccentric orbits, while eliminating it among the lowest E_{rand} particles. Notice that the negligible growth reported by the blue curve reveals that a groove among all the particles having $E_{\text{rand}} \gtrsim 0.04$ has little destabilizing effect.

The perhaps unsurprising conclusion from the new results presented in Figs. 2 and 3 is that groove instabilities are provoked most strongly by deficiencies among the low- E_{rand} particles while groove-like deficiencies among those particles having the most eccentric orbits have little effect on disk stability.

5. INHIBITING SECULAR GROWTH

With these results in hand, we now address the main challenge of this paper.

S12 reported that simulations with particles drawn from our standard DF, without initial grooves, did not remain featureless indefinitely. While simulations with large N did not, at first, support any exponentially growing modes, confirming linear stability predicted by Toomre (1981), all later manifested exponentially growing disturbances. It seemed that shot noise in the disk, amplified by the shear, led to weak collective waves that caused very mild initial resonance scattering, which

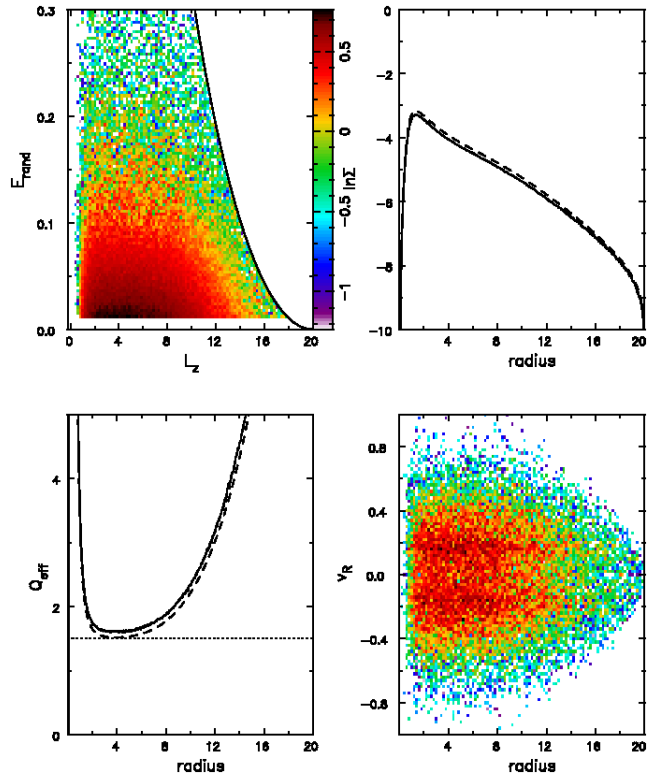


Figure 4. Properties of the particle distribution when those having $E_{\text{rand}} < 0.01$ are excluded from the selection, as illustrated in the top left panel. Eliminating the most nearly circular orbits slightly reduces the disk surface density (top right), raises Q_{eff} , and makes the radial velocity distribution bimodal (bottom right).

“scratched” the DF. The weak scratches caused stronger collective responses in an ever increasing manner until the changes to the DF were sufficient to trigger a genuine instability that then grew exponentially to saturation. Thus the predicted linear stability of the model was undermined by non-linear resonance scattering creating grooves in the DF that eventually led to true instability.

However, we have shown above (§4) that groove instabilities are driven most strongly by deficiencies among the distribution of the low- E_{rand} particles, so if we were to set up a disk in which the lowest E_{rand} particles were removed, the recurrent cycle of scattering that led to the secular growth reported by S12 might be suppressed. In order to test this hypothesis, we selected particles from the standard DF without any grooves while excluding all that had low E_{rand} .

5.1. Excluding low E_{rand} particles

Starting from the standard DF that S12 employed, we eliminated all particles having $E_{\text{rand}} < 0.01$ to obtain the DF shown in Fig. 4. Notice that the surface den-

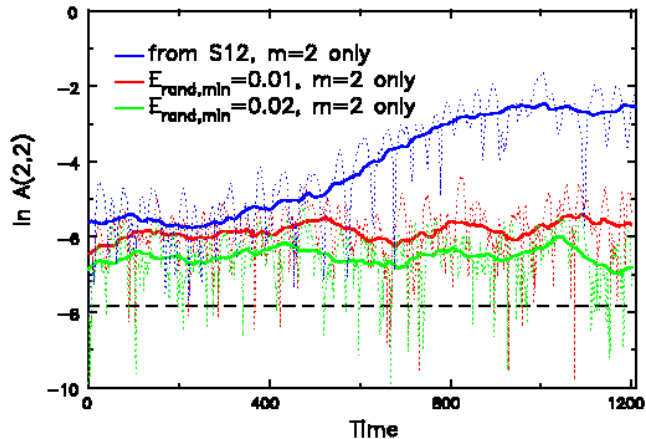


Figure 5. The amplitude evolution of the $m = 2$, $\tan \gamma = 2$ logarithmic spiral component in three simulations. The blue curves are taken from the $N = 5M$ presented in S12 that employed the DF in eq. (1) without a groove. *NB.* Fig. 2 of that paper plots a different measure of the $m = 2$ amplitude. The red line is from the simulation in which particles with $E_{\text{rand}} < 0.01$ were excluded from selection, as shown in Fig. 4, while the green line is from a simulation that lacked particles with $E_{\text{rand}} < 0.02$ in which activity is even more subdued. Notice that secular growth is eliminated in both these cases

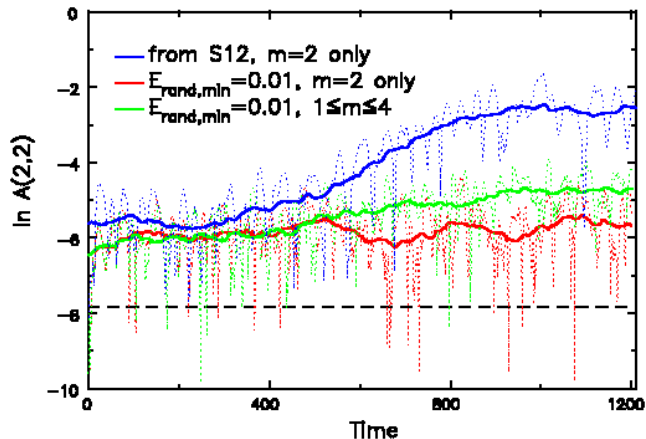


Figure 6. The red and blue lines are the same as those fig. 5, but the green line is a rerun of the same DF used for the red line with forces from $1 \leq m \leq 4$ active.

sity is reduced by $\sim 11.6\%$, Q is slightly increased, and the distribution of radial velocities becomes bimodal, as shown in the top right, bottom left, and the bottom right panels respectively.

Using this DF, we obtained the amplitude evolution of the largest trailing bisymmetric component, the usual $m = 2$, $\tan \gamma = 2$, which we compare in Fig. 5 with the result shown by the blue line previously reported by S12 for the same N that included particles for all $E_{\text{rand}} \geq$

Table 2. Default numerical parameters for 3D

Grid points in (r, ϕ, z)	$220 \times 256 \times 125$
Vertical spacing of planes	$0.04R_0$
Grid scaling	$R_0 = 10$ grid units
Active sectoral harmonics	$m = 0\&2$ or $m = 0, 2, 3\&4$
Softening length	$\epsilon = R_0/10$
Number of particles	5×10^6 or 5×10^7
Largest time-step	$0.08R_0/V_0$
Radial time step zones	5
Guard radii	4

0. (Note that a different measure of the amplitude was plotted in Fig. 2 of the earlier paper.) These simulations were run for six times longer than those presented in Figs. 2 and 3. The red and green lines, which manifest no secular growth, report the results when $E_{\text{rand}} \geq 0.01$ and 0.02 respectively. The disk is a bit more lively with the smaller lower bound on E_{rand} , but even this case secular growth was suppressed.

These results were obtained from simulations in which disturbance forces were restricted to $m = 2$, and it is of interest to determine whether secular growth is also suppressed when disturbance forces from multiple sectoral harmonics are active. The green line in Fig. 6 plots the $m = 2$ amplitude from a simulation that has the same DF given by the red line, but in which disturbance forces from $1 \leq m \leq 4$ were active. The green line in this Figure is slightly higher than the red, and the $m = 1$ and $m = 3$ amplitudes also rose at a similar very slow rate.

It should be admitted, however, that the DF for this model with negligible secular growth seems unnatural because the radial velocity distribution is bimodal (see Fig. 4).

6. ALLOWING 3D MOTION

All the results presented so far, as well as the prediction from Toomre (1981), relate to a razor-thin disk. However, real galaxies have disks of finite thickness. Toomre (1982) describes a family of exact axisymmetric, thickened disk models having similar properties to those of the razor-thin Mestel disk, but they all pinch down to zero thickness at the center, while being particularly puffy at intermediate radii, and therefore do not make realistic 3D generalizations of the Mestel disk. Instead, we need to construct a 3D disk that resembles the half-mass Mestel disk model and which is close to equilibrium.

6.1. Setting up a thickened Mestel disk

Our standard DF used by Toomre (1981) (eqs. 1 & 3) yields a suitable set of particles in a razor thin disk,

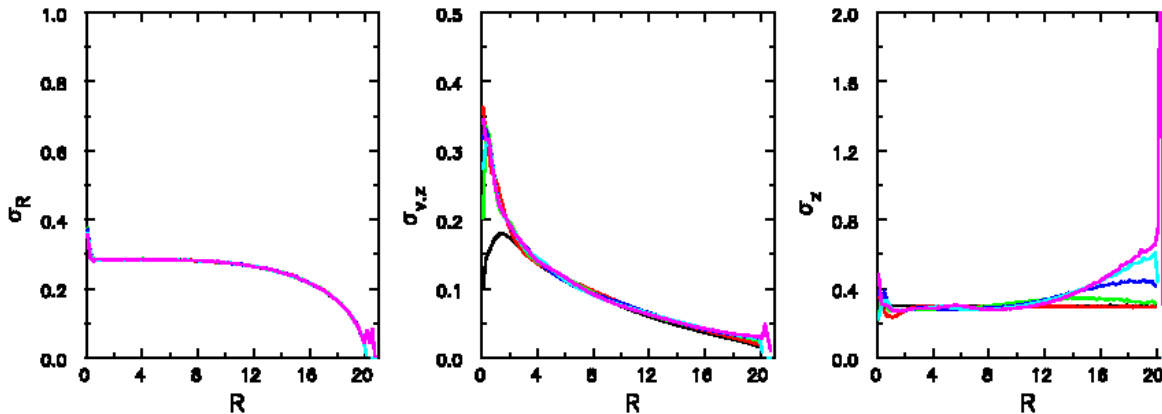


Figure 7. The initial flaring of the 3D disk. The left hand and middle panels show the radial and vertical velocity dispersions of the disk particles at $t = 0$ (black) and at intervals of 6 time units in order red, green, blue, cyan, and magenta. The right hand panel shows the rms disk thickness increases at radii $R > 10$ at the same times, but there is no further thickening after $t = 30$.

which we can spread vertically as a Gaussian in z to create the density distribution

$$\rho(R, z) = \frac{\Sigma(R)}{(2\pi)^{1/2} z_0} \exp\left(-\frac{z^2}{2z_0^2}\right), \quad (8)$$

with $z_0 = 0.3R_0$ being the disk scale height that is independent of R . But achieving both radial and vertical balance presents a number of challenges.

The first challenge is that we must allow for forces that are not confined to the disk plane. With a 2D model, we could simply establish equilibrium by setting the total central attraction to $a_R = -V_0^2/R$, without any axisymmetric contribution from self-consistent forces. Notionally, we can think of half of this force as arising from the attraction of the halo, because the disk mass was halved, and the other half from a smooth razor-thin, semi-infinite disk. In 2D disks, it does not matter how the attractions of these two components might vary out of the $z = 0$ plane, but it does for a thickened disk.

The thin disk particles have in-plane velocity components that create an equilibrium model if the in-plane attraction were $-V_0^2/R$ at all distances from the mid-plane. (R is the cylindrical radius.) The initial, vertically-spread, particle distribution is axisymmetric and therefore their gravitational attraction computed through the grid would be also. We first use a 3D grid, with parameters in Table 2, to obtain the gravitational field of the disk particles in their initial positions and compute their azimuthally averaged central attraction $a_{R,\text{grid}}(R, z)$ at every grid point. We then preserve, in a separate copy of the grid, the value $-V_0^2/R - a_{R,\text{grid}}(R, z)$ and apply this correction to the grid-determined forces from the particles at each grid point at each time step to preserve the radial balance.

The grid-determined vertical attraction from the disk particles will be considerably less than it should be because of softened gravity and the fact that the tapers have removed a lot of mass. However, we do not have to try to reproduce the exact vertical forces; they need to be strong enough only to require vertical velocities large enough to inhibit buckling instabilities over most of disk. We therefore add to the vertical force the vertical component of the attraction from the, assumed spherical, half-mass halo: $-V_0^2 z/(2r^2)$, where r is the spherical radius and z the distance from the mid-plane.

With the total gravitational attraction now available, the final step before starting the simulation is to set the vertical velocities of the disk particles. We integrate the vertical 1D Jeans equation (Binney & Tremaine 2008, eq. 422b) for a slab, *i.e.* neglecting radial variations. In this case

$$\sigma_{v_z}(R, z) = \frac{1}{\rho(R, z)} \int_z^\infty \rho(R, z') \frac{\partial \Phi}{\partial z} dz', \quad (9)$$

where the vertical gradient of the total potential Φ is determined numerically from the active particles, as well as the rigid mass components. This formula yields an acceptable equilibrium when, as here, the radial excursions of disk particles are small; we do not need the Stäckel approximation recommended for hotter disks by Sanders & Binney (2016).

This set-up procedure yields a model in near perfect balance with the initial virial ratio being 0.4953.

6.2. Flaring

As noted in the introduction, 3D motion allows for the possibility of buckling instabilities that are caused by too large a disparity between the radial and vertical velocity dispersions in the disk. The radial variations

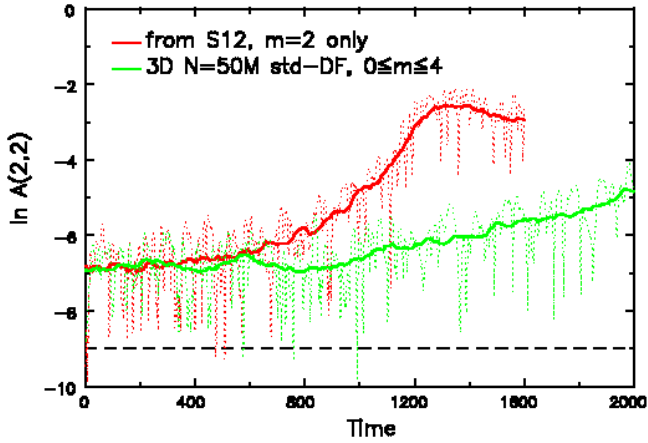


Figure 8. Comparison of the amplitude evolution of the standard DF in 2D (red) and 3D (green). The red line is the $N = 50M$ case from S12, which used the standard DF with no groove. The green line is from a model that uses the same DF but which was run with $0 \leq m \leq 4$ force terms on the 3D polar grid. The amplitude rises in both simulations, though more slowly in 3D.

of the initial radial and vertical velocity dispersions of our model are indicated by the black lines in the left and middle panels of Fig. 7, with the colored lines being the same measurements at intervals of 6 time units from the start revealing little change – *i.e.* the model is very close to radial and vertical equilibrium. The DF parameter $q = 11.44$ (eq. 1) sets $\sigma_R = 0.284$ over the inner disk, which decreases at larger R because larger E_{rand} particles are eliminated by the outer truncation – see Fig. 1.

The vertical velocity dispersion is set to support the adopted constant initial disk thickness $z_0 = 0.3$ in the gravitational field of the model (see eq. 9), which causes the vertical dispersion to decrease below 0.1 for $R \gtrsim 10$, and therefore to drop below the threshold for buckling instability $3\sigma_{v_z} \lesssim \sigma_R$ Araki (1987). The consequence is that the outer disk begins gradually to flare due to a local buckling instability. The modest increase in σ_z for $R < 20$, right panel, gradually asymptotes to its final profile at $t \simeq 30$, and no further increase was detectable for the remainder of the evolution. It is remarkable how small an increase in the vertical velocity dispersion, middle panel of Fig. 7, is required to relieve this particular instability.

6.3. Standard DF

Fig. 8 compares the amplitude evolution of the $m = 2$, $\tan \gamma = 2$ logarithmic spiral component in 2D and in 3D. Both runs start from the standard DF without a groove and manifest secularly growing amplitude, which is slower in 3D, probably because the gravity of distur-

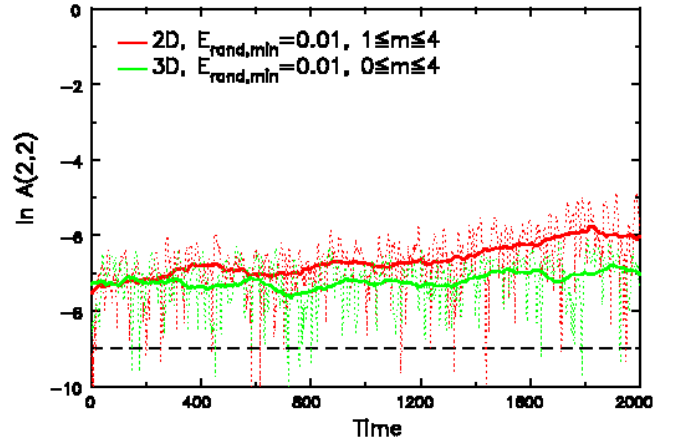


Figure 9. As for Fig. 8 with $N = 50M$, but for the modified DF with particles having $E_{\text{rand}} < 0.01$ eliminated. The red line is from the same simulation as the green line in Fig. 6, but continued to later times.

bances is weakened by spreading the particles vertically. However, the qualitative evolution appears to be unchanged by allowing 3D motion and including multiple secular harmonics in the disturbance forces.

6.4. Eliminating low- E_{rand} particles

Fig. 6 showed that the DF in Fig. 4 stopped secular growth in 2D simulations. Fig. 9 confirms that this result is unchanged when 3D motion is allowed. Although we stopped the 3D simulation in Fig. 8 before the non-axisymmetric disturbances had saturated, the steady rise of the green curve there contrasts strongly with the flat behavior of the green curve in Fig. 9, indicating a clear difference between stable and mildly unstable cases.

7. DISCUSSION

The sequence of events, described in §1, that gives rise to secular growth in simulations with the standard DF is closely related to the recurrent cycle of groove modes proposed by Sellwood & Carlberg (2019) to account for the transient spirals that develop spontaneously in simulations of bar-stable disks. A groove causes exponential growth of a spiral which stores the angular momentum extracted from the disk as its amplitude grows. As the mode decays the L_z stored in the spiral drains onto the Lindblad resonances (Sellwood & Carlberg 2022), which carves new grooves at some radial distance from the original. The new grooves cause more spiral instabilities, increasing random motion throughout the disk, causing activity to subside in the absence of cooling by gas (Sellwood & Carlberg 1984).

Thus gas-free disks are eventually stabilized when Q has risen to a value that weakens collective spiral insta-

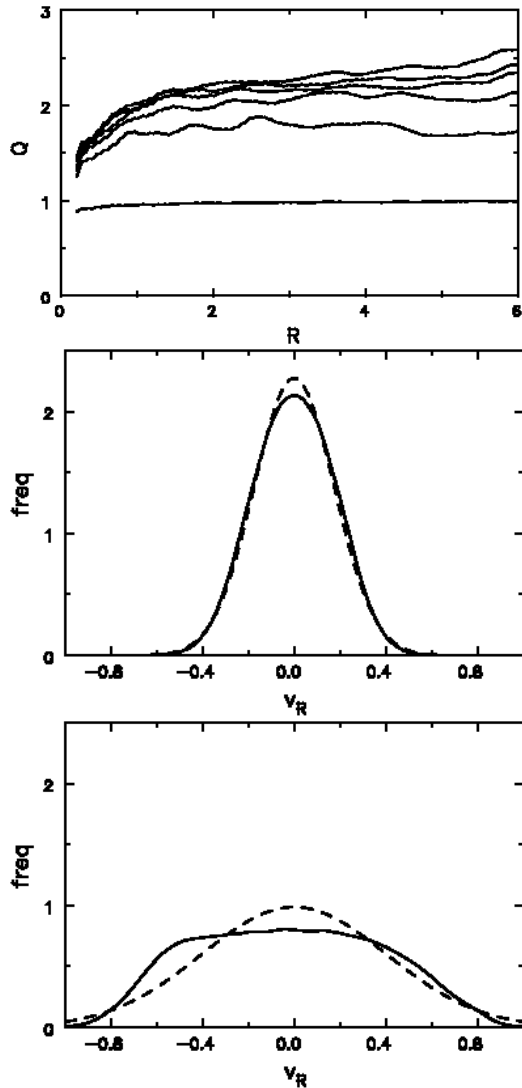


Figure 10. Top: The evolution of Q taken from a 2D, $N = 2M$ simulation of an SC disk model from Sellwood & Carlberg (2014). The lines show the radial variation of Q at times 0(200)1000 time units.

Middle: The solid curve shows the distribution of radial velocities of all $\sim 950K$ particles in the disk within the annulus $1 \leq R \leq 4$ at $t = 1000$. The dashed curve shows a Gaussian distribution having the same mean and σ . Notice that the velocity distribution is not quite as peaked as a Gaussian.

Bottom: A similar plot to the middle panel, but from the region around the ILR of simulation that supported a strong spiral. The spiral was triggered by a groove in the Mestel disk and was reported in (Sellwood & Carlberg 2022).

bilities, typically when $Q \gtrsim 2$, as shown by the time convergence of the lines in the top panel of Fig. 10. The middle panel shows the distribution of radial velocities in the disk at the last moment, which is less strongly peaked than a Gaussian. The velocity distribution presented in the bottom panel resulted from scattering at

the ILR of the strong spiral described in the paper by Sellwood & Carlberg (2022). This more dramatically non-Gaussian distribution is that at $t = 360$, for which the distribution in action space was illustrated in Fig. 4 of their paper. These lower two panels reveal that spiral scattering depletes near circular orbits, which is particularly pronounced for a strong spiral. While the depletion is not total, as it was for the DF (Fig. 4) used in Figs. 6 and 9, we suspect it will have a reduced, but similar, stabilizing effect.

8. CONCLUSIONS

Previous work by Toomre (1981), described in §1, had found that the half-mass Mestel disk having a gentle central cutout and outer taper, possessed no small-amplitude instabilities, and was therefore expected to be stable. Sellwood (2012) confirmed, in large- N simulations that there were no *linear* instabilities, but found unexpectedly that his simulations always manifested secular growth by non-linear resonant scattering, described in §1, which undermined Toomre’s prediction of disk stability.

Our present study (§4) of groove instabilities confirmed our earlier suspicions that instability is provoked more strongly by removing particles of low- E_{rand} , than by those having more eccentric orbits. Since the secular rise of amplified noise is driven by grooves/scratches in the DF, we suspected that removing all particles having small E_{rand} from the DF might inhibit the secular growth reported by Sellwood (2012), and indeed it did, as we found in Figs 5 and 6.

Here we extend our study of the instabilities of the Mestel disk to 3D for the first time. While achieving an equilibrium model from which to start our simulations was hard, we found that motion in 3D made little difference to the in-plane behavior. The outer edge of the tapered and truncated disk did support a mild buckling instability, however, which ran its course quickly leaving the outer disk mildly flared, but otherwise little changed.

Lack of growth in simulations is not, of course, proof of absolute stability – we can merely place an upper bound on the growth rate of non-axisymmetric disturbances. Since the orbit period at $r = 6$ is ~ 37 time units, the duration of the simulations in Fig.9 is over 50 orbits. So it seems reasonable to conclude that secular growth in our modified Mestel disk model is negligible.

We note that our study has excluded a possible gas component within the disk. This neglect is appropriate, however, because we are addressing the stability of featureless disks, such as those in S0 galaxies, which are believed to have very low gas content.

The rigid halo in our models is an important contributor to disk stability and we have not here tested whether replacing it with mobile particles would destabilize the entire model. However, in a direct test of this issue, Sellwood (2021) concluded that spiral disturbances in a disk do not couple to a halo composed of mobile particles. However, we caution the reader that if there were a mild bar instability in a disk embedded in a rigid halo, a responsive halo may well increase the growth rate of the instability.

One might worry that our finding that secular growth can be inhibited by removing low- E_{rand} particles may have little relevance to the stability of real galaxies, since it requires a DF that is non-Gaussian in radial velocities (Fig. 4). However, the DF of a galaxy disk is sculpted over time by resonant scattering, which depletes the

density of low E_{rand} particles. Sellwood & Carlberg (1984) argued that star formation to replenish low E_{rand} stars was essential to maintain spiral activity in a disk, whereas here we are using a similar argument that a disk galaxy can be stable if there are few low E_{rand} stars – they having been depleted by earlier spiral activity, that has now abated when the supply of fresh gas has been removed. We show in Fig. 10 that the spiral scattering does indeed introduce negative kurtosis into the velocity distribution, which can be quite pronounced in the case of strong spirals, and that change will inevitably add to the stability of the entire disk.

We thank an anonymous referee for a careful read of the paper and an insightful report. JAS acknowledges the continuing hospitality and support of Steward Observatory.

REFERENCES

- Araki, S. 1987, *AJ*, **94**, 99
- Athanassoula, E. & Sellwood, J. A. 1986, *MNRAS*, **221**, 213
- Binney J. & Tremaine S. 2008, *Galactic Dynamics* 2nd ed. (Princeton University Press, Princeton NJ)
- De Rijcke, S., Fouvy, J-B. & Pichon, C. 2019, *MNRAS*, **484**, 3198
- Erwin, P. 2018, *MNRAS*, **474**, 5372
- Fouvy, J-B. & Pichon, C. 2015, *MNRAS*, **449**, 1982-95
- Hohl, F. 1971, *ApJ*, **168**, 343
- Kalnajs, A. J. 1972, *ApJ*, **175**, 63
- Kalnajs, A. J. 1978, in *IAU Symposium 77 Structure and Properties of Nearby Galaxies* eds. E. M. Berkhuisjen & R. Wielebinski (Dordrecht:Reidel) p. 113
- Lynden-Bell, D. & Kalnajs, A. J. 1972, *MNRAS*, **157**, 1
- Mark, J. W-K. 1974, *ApJ*, **193**, 539
- Merritt, D. & Sellwood, J. A. 1994, *ApJ*, **425**, 551
- Papaloizou, J. C. B. & Lin, D. N. C. 1989, *ApJ*, **344**, 645
- Polyachenko, V. L. 1977, *Pis'ma Astron. Zh.*, **3**, 99; English translation: *Sov. Astr. Lett.* **3**, 51
- Sanders, J. L. & Binney, J. 2016, *MNRAS*, **457**, 2107
- Sellwood, J. A. 2012, *ApJ*, **751**, 44 (S12)
- Sellwood, J. A. 2014, arXiv:1406.6606 (on-line manual: <http://www.physics.rutgers.edu/~sellwood/manual.pdf>)
- Sellwood, J. A. 2021, *MNRAS*, **506**, 3018
- Sellwood, J. A. 2024, *MNRAS*, **529**, 3035
- Sellwood, J. A. & Binney, J. J. 2002, *MNRAS*, **336**, 785
- Sellwood, J. A. & Carlberg, R. G. 1984, *ApJ*, **282**, 61
- Sellwood, J. A. & Carlberg, R. G. 2014, *ApJ*, **785**, 137
- Sellwood, J. A. & Carlberg, R. G. 2019, *MNRAS*, **489**, 116
- Sellwood, J. A. & Carlberg, R. G. 2022, *MNRAS*, **517**, 2610
- Sellwood, J. A. & Carlberg, R. G. 2023, *ApJ*, **958**, 182
- Sellwood, J. A. & Kahn, F. D. 1991, *MNRAS*, **250**, 278
- Sellwood, J. A. & Lin, D. N. C. 1989, *MNRAS*, **240**, 991
- Sellwood, J. A. & Masters, K. L. 2022, *ARA&A*, **60**, 73
- Sellwood, J. A. & Merritt, D. 1994, *ApJ*, **425**, 530
- Toomre, A. 1966, in *Geophysical Fluid Dynamics*, notes on the 1966 Summer Study Program at the Woods Hole Oceanographic Institution, ref. no. 66-46, p 111
- Toomre, A. 1977, *ARA&A*, **15**, 437
- Toomre, A. 1981, In *The Structure and Evolution of Normal Galaxies*, eds. S. M. Fall & D. Lynden-Bell (Cambridge, Cambridge Univ. Press) p. 111
- Toomre, A. 1982, *ApJ*, **259**, 353
- Toomre, A. & Kalnajs, A. J. 1991, in *Dynamics of Disc Galaxies*, ed. B. Sundelius (Gothenburg: Göteborgs University) p 341
- Zang, T. A. 1976, PhD thesis., MIT